

SYNTHESIS AND CHARACTERIZATION OF $\text{Li}[\text{Mn}_{2-x}\text{Mg}_x]\text{O}_4$ ($x = 0.0-0.3$) PREPARED BY SOL-GEL SYNTHESIS

PRITI SINGH, ANJAN SIL*, MALA NATH, SUBRATA RAY*

*Department of Chemistry, Indian Institute of Technology Roorkee,
Roorkee 247667, India*

**Department of Metallurgical and Materials Engineering,
Indian Institute of Technology Roorkee, Roorkee 247667, India*

E-mail: anj_sil@yahoo.co.uk

Submitted September 21, 2009; accepted January 5, 2010

Keywords: Ceramic oxide; Sol-gel technique; X-ray diffraction; Thermogravimetric analysis

XRD analysis of $\text{Li}[\text{Mn}_{2-x}\text{Mg}_x]\text{O}_4$ ($x = 0.0, 0.05, 0.1, 0.15, 0.2, 0.25$ and 0.3) powders synthesized by a sol-gel process, shows single phase cubic spinel structure having space group $Fd\bar{3}m$ up to $x = 0.25$. When Mg content increases to $x = 0.3$, second phase with space group $P4_332$ appears. TG (Thermo Gravimetric) analysis shows the oxygen loss from the structure begins at lower temperature as the Mg content increases. DTA (Differential Thermogravimetric Analysis) shows stabilization of orthorhombic LiMnO_2 and tetragonal Mn_3O_4 by Mg doping. Number of vibrational bands increase as the Mg content increases which indicate that the ordering of spinel structure increases and the reduction of the space group from O_h^h ($Fd\bar{3}m$) to O^f ($P4_332$). The discharge capacity of 122 mAh g^{-1} has been observed for LiMn_2O_4 and it decreases when the increase in Mg content. In Mg doped samples $\text{Li}[\text{Mn}_{2-x}\text{Mg}_x]\text{O}_4$, step corresponding to cubic-cubic transition decreases and gets completely removed for $x = 0.25$.

INTRODUCTION

In rechargeable lithium-ion battery available in market, LiCoO_2 is often used as cathode and LiC_6 as anode materials. The choice of these materials as hosts for lithium intercalation is due to their layered structures as demonstrated by the pioneering investigations of Basu et al. [1] for anode and of Goodenough et al. [2] for cathode. However, LiCoO_2 is expensive due to limited source of this material and is also toxic in nature. Therefore, there are efforts worldwide to search for alternate host material for cathode. Lithium Manganese oxides, which are non-toxic, manganese being abundantly available and cost effective, appear to be a potential candidate for application in lithium-ion battery as cathode material. But lithium manganese oxide has not layered rhombohedral structure like LiCoO_2 [3]. In LiMn_2O_4 , lithium ions occupies 8a tetrahedral sites, manganese ions are at 16d octahedral sites and oxygen ions are arranged at 32 e forming cubic close packed structure. In the spinel $\text{Li}_x\text{Mn}_2\text{O}_4$, structural transformation occurs during the electrochemical reaction. $\text{Li}_x\text{Mn}_2\text{O}_4$ with $0 < x \leq 1$, remains in a cubic spinel structure at 4 V. On the other hand, when $1 < x \leq 2$ phase transition occurs from cubic to tetragonal structure at about 3 V [4]. In the 3 V range, a drastic capacity loss with cycling is observed due to the structural transition from cubic to

tetragonal. This transition is derived from the Jahn-Teller active $\text{Mn}^{3+}(3d^4)$ ions. Capacity fading is also caused due to lattice instability, dissolution of manganese into the electrolyte, oxidation of the electrolyte, formation of oxygen rich spinel and particle disruption [5, 6]. In order to improve the cyclic performance of spinel LiMn_2O_4 in the 4 V range, manganese atom was partially replaced by transition metal Mg, Zn, Fe, Ni, Zn, Cr, Co [7-9].

Until recently, the spinel lithium manganese oxide and the substituted compounds have been prepared mainly by solid-state reactions, sol-gel method, Pechini process, hydrothermal route and emulsion method [10]. Sol-gel processing method has several advantages such as good control on powder stoichiometry, requirement of lower calcination temperature and relatively low processing time and synthesis of submicron sized particle with narrow particle size distribution. It is well known that the electrochemical performance of the electrode is strongly affected by the powder properties, such as the particle morphology, the specific surface area and crystallinity of the powders. In the present work spinel compound $\text{Li}[\text{Mn}_{2-x}\text{Mg}_x]\text{O}_4$ ($x = 0.0, 0.05, 0.1, 0.15, 0.2, 0.25$ and 0.3) were prepared by sol-gel synthesis using citric acid as a chelating agent. The physical characterizations and the electrochemical performances of these synthesized powders are reported in this article.

EXPERIMENTAL

Materials preparation and characterization

The $\text{Li}[\text{Mn}_{2-x}\text{Mg}_x]\text{O}_4$ ($x = 0.0, 0.05, 0.1, 0.15, 0.2, 0.25$ and 0.3) powders have been synthesized by sol-gel method using citric acid as a chelating agent. The stoichiometric amount of raw materials i.e. lithium acetate, manganese acetate, and magnesium acetate were used as starting materials to prepare the precursor. The ratio of metal ions to citric acid was kept nearly 1.0. The acetates were dissolved separately in appropriate quantities of distilled water and mixed. Saturated aqueous solution of citric acid prepared separately was added drop by drop in the acetate mixture to convert it into transparent sol. A clear transparent sol was formed and converted to clear gel (viscous) by continuously stirring and heating at $100-120^\circ\text{C}$. The pH of the mixed solution was adjusted between 6-7 by adding ammonia solution. The gel was dried at 140°C for 3-4 h in order to obtain the precursor powder. The powder was then calcined at about 750°C for 15 h, ground and re-calcined at 750°C for 5 h in air. Heating and cooling rate was maintained at $1^\circ\text{C}/\text{min}$.

Thermal analysis (DTA and TG) of the samples were carried out by a thermal analyzer (Perkin Elmer, Pyris Diamond) with alumina as a reference material and heating at the rate of $10^\circ\text{C}/\text{min}$ in presence of air. The structure and phase contents of the samples were examined by X-ray diffraction analysis in powder diffractometer using $\text{CuK}\alpha$ radiation and the measurement range was $10-90^\circ$ with 0.02° step size and scan step time 0.5 second. Stripping of $\text{CuK}\alpha_2$ radiation was performed during the analysis. Structure parameters and lattice parameter were obtained by using the Rietveld method with the X'Pert HighScore Plus software.

Infrared spectra of the samples were recorded in a Thermo Nicolet (Anexus) at room temperature on a FTIR 1600 series. The sample powder was ground along with potassium bromide (Aldrich, 99.9 %) and the powder mixture was pressed at a load of 10 tons in a die having rectangular area 1×4 cm. The morphology of the powders was observed by Field emission scanning electron microscope (FEI QUANTA 200 F). Image J software was used to determine average particle size of the samples from the micrographs.

Electrochemical properties

Electrode preparation, cell construction, and sealing were carried out in an argon filled glove box (MBRAUN-MB 200G) having < 1.0 ppm oxygen concentration. Positive electrode was made by mixing 70 % active material, 15 % polyvinylidene difluoride (PVDF) binder and 15 % acetylene black in N-methyl-2-pyrrolidone (NMP) solvent. Mixed slurry diluted in NMP was uniformly spread by using doctor-blade on

one side of aluminum foil of known weight and dried at 140°C for 24 hours in vacuum oven. The foil with paste was then rolled and dried again for 2 hours. The mass of the active material (cathode) was determined from the difference in weight of aluminum foil and foil with paste. The electrochemical measurements were carried out by constructing a teflon cell with a small piece of lithium foil as negative electrode. The electrolyte used was 1M LiPF_6 dissolved in a 1:1 vol.% mixture of ethylene carbonate and diethyl carbonate and polypropylene films were used as separator. The cell was tested at constant current (100 mA) by using computer controlled system between 3.0 and 4.3 V at 20°C .

RESULTS AND DISCUSSION

Structure identification by X-ray diffraction analysis

Figure 1 shows Rietveld refinement of the oxide powder in $\text{Li}[\text{Mn}_{2-x}\text{Mg}_x]\text{O}_4$ ($x = 0.0, 0.05, 0.1, 0.15, 0.2, 0.25$ and 0.3). In order to determine cell parameters the XRD patterns were analysed by Rietveld refinement method. Two models were used for the refinement. In the first model, atomic arrangement is in accordance with $\text{Fd}3\text{m}$ space group symmetry, while the second model involved ordered spinel structure with the space group symmetry $\text{P}4_332$. Refinement parameters such as R_{exp} (expected), R_p (profile), R_{wp} (weighted profile) and GOF (Goodness of fit) for the patterns analyzed are given in Table 1, while the structural parameters are contained

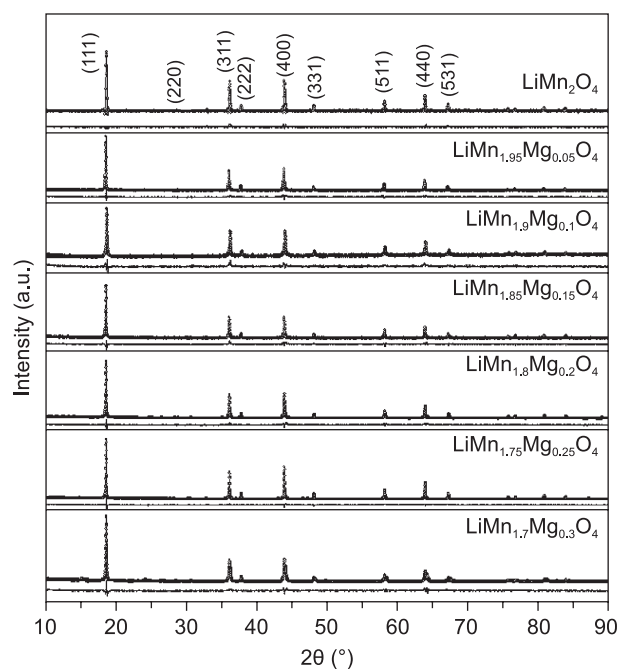


Figure 1. Rietveld refinement plots - observed data points are shown as filled circle (●) and calculated data points by unfilled circle (○) and difference plots are shown at bottom.

in Table 2. The powders having compositions up to $x = 0.25$ are found to have single-phase of cubic spinel structure having space group Fd3m. In this structure the lithium ions occupy the tetrahedral (8a) sites and manganese and magnesium ions reside at the octahedral

(16d) sites. It has been reported that in the cubic spinel $\text{Li}[\text{Mn}_{2-x}\text{Mg}_x]\text{O}_4$, two space groups Fd3m and P4₃32 coexist for $x = 0.25$ [11]. In the present study, the phase analysis of the compound at $x = 0.25$ shows that phase having P4₃32 space group is negligibly small, and for

Table 1. Results for Rietveld refinement of $\text{Li}[\text{Mn}_{2-x}\text{Mg}_x]\text{O}_4$ ($x = 0.0, 0.05, 0.1, 0.15, 0.2, 0.25$ and 0.3).

Composition	Lattice parameter (Å)	R_{exp} (%)	R_{wp} (%)	R_{p} (%)	GOF	R_{Bragg} (%)
LiMn_2O_4	8.2400	7.820	6.665	5.233	0.726	2.852
$\text{LiMg}_{0.05}\text{Mn}_{1.95}\text{O}_4$	8.2367	4.209	4.600	3.516	1.194	2.0465
$\text{LiMg}_{0.1}\text{Mn}_{1.9}\text{O}_4$	8.2365	4.803	5.293	3.934	1.214	3.733
$\text{LiMg}_{0.15}\text{Mn}_{1.85}\text{O}_4$	8.2306	4.283	5.086	3.852	1.409	5.506
$\text{LiMg}_{0.2}\text{Mn}_{1.8}\text{O}_4$	8.2300	4.235	4.537	3.505	1.148	1.622
$\text{LiMg}_{0.25}\text{Mn}_{1.75}\text{O}_4$	8.2290	4.245	4.239	3.326	0.997	1.890
$\text{LiMg}_{0.3}\text{Mn}_{1.7}\text{O}_4$	–	4.279	5.841	4.020	1.863	–
Fd3m (48 %)	8.2218	–	–	–	–	6.558
P4 ₃ 32 (52 %)	8.1871	–	–	–	–	6.674

Table 2. Structural parameters of $\text{Li}[\text{Mn}_{2-x}\text{Mg}_x]\text{O}_4$ ($x = 0.0, 0.05, 0.1, 0.15, 0.2, 0.25$ and 0.3).

Phase	Atom	Wyckoff Positions	Site occupancy factor (s.o.f.)	Coordinates		
				x	y	z
LiMn_2O_4	Li	8a	1.0000	0.1250	0.1250	0.1250
	Mn	16d	1.0000	0.5000	0.5000	0.5000
	O	32e	1.0000	0.2560	0.2560	0.2560
$\text{LiMg}_{0.05}\text{Mn}_{1.95}\text{O}_4$	Li	8a	1.0000	0.1250	0.1250	0.1250
	Mn	16d	0.9750	0.5000	0.5000	0.5000
	Mg	16d	0.0250	0.5000	0.5000	0.5000
	O	32e	1.0000	0.2570	0.2570	0.2570
$\text{LiMg}_{0.1}\text{Mn}_{1.9}\text{O}_4$	Li	8a	1.0000	0.1250	0.1250	0.1250
	Mn	16d	0.9500	0.5000	0.5000	0.5000
	Mg	16d	0.0500	0.5000	0.5000	0.5000
	O	32e	1.0000	0.2500	0.2500	0.2500
$\text{LiMg}_{0.15}\text{Mn}_{1.85}\text{O}_4$	Li	8a	1.0000	0.1250	0.1250	0.1250
	Mn	16d	0.9250	0.5000	0.5000	0.5000
	Mg	16d	0.0750	0.5000	0.5000	0.5000
	O	32e	1.0000	0.2560	0.2560	0.2560
$\text{LiMg}_{0.2}\text{Mn}_{1.8}\text{O}_4$	Li	8a	1.0000	0.1250	0.1250	0.1250
	Mn	16d	0.9000	0.5000	0.5000	0.5000
	Mg	16d	0.1000	0.5000	0.5000	0.5000
	O	32e	1.0000	0.2560	0.2560	0.2560
$\text{LiMg}_{0.25}\text{Mn}_{1.75}\text{O}_4$	Li	8a	1.0000	0.1250	0.1250	0.1250
	Mn	16d	0.8750	0.5000	0.5000	0.5000
	Mg	16d	0.1250	0.5000	0.5000	0.5000
	O	32e	1.0000	0.2560	0.2560	0.2560
$\text{LiMg}_{0.3}\text{Mn}_{1.7}\text{O}_4$	Li	8a	1.0000	0.1250	0.1250	0.1250
	Mn	16d	0.8500	0.5000	0.5000	0.5000
	Mg	16d	0.1500	0.5000	0.5000	0.5000
	O	32e	1.0000	0.2560	0.2560	0.2560
Fd3m	Li	8c	1.0000	0.7900	0.7900	0.7900
	Mg1	4a	0.6000	0.3750	0.3750	0.3750
	Mn	12d	1.0000	0.1250	0.1210	0.3710
	Mg2	12d	0.1330	0.1250	0.1210	0.3710
	O1	8c	1.0000	0.1350	0.1350	0.1350
	O2	24e	1.0000	0.1268	0.3540	0.3580

$x = 0.30$ the P4₃2 phase content becomes about 52 % (by weight) and is present along with the cubic spinel Fd3m phase as given in Table 1. Since the characteristic peaks of the compounds lie in the range 55–70°, XRD data at lower range are shown in Figure 2. When $x = 0.3$ in $\text{Li}[\text{Mn}_{2-x}\text{Mg}_x]\text{O}_4$, new peaks corresponding to P4₃2 space group appears (Figure 2). For pure cubic spinel LiMn_2O_4 the (220) peak has negligibly low intensity (less than 1% of the highest intensity peak). Moreover, Ohzuku et al. [12] suggested that the intensity of (220) peak increases if the substituted metal ion occupies the tetrahedral 8a site. It can be seen from Figure 1 that intensity enhancement at the (220) peak position has not occurred by successive substitutions with increasing Mg content. Therefore it can be attributed that the Mg substitution in the cubic spinel does not occupy tetrahedral 8a sites and instead all the Mg ions can be taken as occupied in the 16d sites. This has also been confirmed by the Rietveld refinement of the relevant pattern. Rietveld analyses carried out separately by assigning the Wyckoff position of Mg to 8a sites in one case and to 16d sites in another, have shown that the difference plots become more flatter for 16d sites occupancy than the case with 8a sites.

Lattice parameter of the unit cells for the compounds are given in Table 1. A gradual decrease in lattice parameter is observed with increasing x . This is due to the difference in ionic radii of Mn^{3+} and Mn^{4+} . When Mg^{2+} was doped to the site of Mn^{3+} (ionic radius 0.79 Å) in the spinel structure, the number of Mn^{4+} (ionic radius 0.67 Å) increases in order to maintain the charge balance condition. Thus lattice parameter of the unit cell decreases with the increase in Mg content.

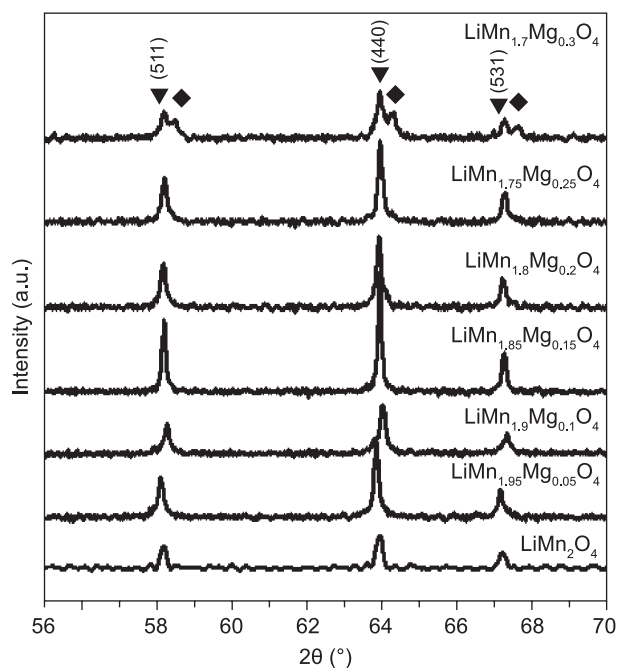
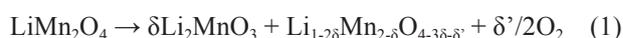


Figure 2. XRD patterns between 2θ range 55–70°. (▼ - Fd3m space group, ◆ - P4₃2 space group)

TG-DTA analysis

Figure 3 shows the TG traces of $\text{Li}[\text{Mn}_{2-x}\text{Mg}_x]\text{O}_4$ with $x = 0.00, 0.05, 0.1, 0.15, 0.20, 0.25$ and 0.30 generated between room temperature and 1300 °C. It can be seen from the figure that there exists two temperatures T_1 and T_2 at which mass loss is significant. The mass loss is associated with loss of oxygen from the spinel accompanied by lithium diffusion to the particle surface where disproportionation reaction occurs [11, 13]. This results in the formation of Li_2MnO_3 and tetragonal spinel in which manganese ions reduced to an oxidation state below 3.5. The amount of oxygen loss and the increase in concentration of Mn^{3+} cause the tetragonal distortion in the structure. The overall reaction that occurs between T_1 to T_2 is there proposed to be



Oxygen is lost rapidly from the sample above T_2 . In this reaction Li_2MnO_3 phase is consumed by the manganese-rich spinel phase to produce LiMnO_2 . The overall reaction at above T_2 is represented by the following equation:

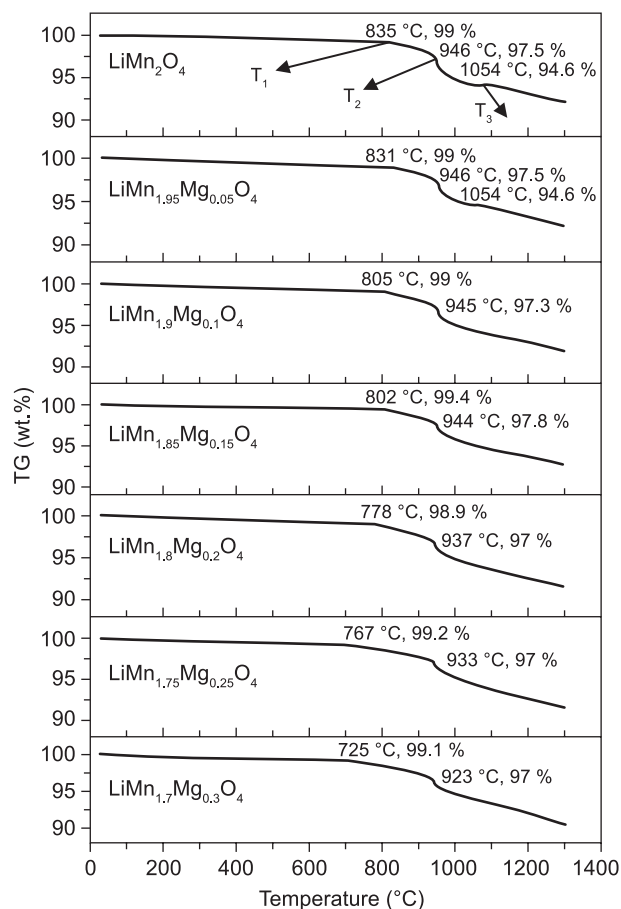
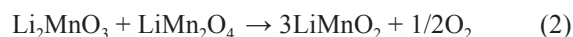


Figure 3. TGA plots of $\text{Li}[\text{Mn}_{2-x}\text{Mg}_x]\text{O}_4$ where $x = 0.00, 0.05, 0.10, 0.15, 0.20, 0.25, 0.30$.

It is seen from the TG plots in Figure 3 that the transition T_1 shifts toward the lower temperature as the Mg content increases showing that the oxygen loss from the spinel structure begins at lower temperature with Mg substitution. This is due to bond enthalpy of the Mg–O (bond enthalpy = 363 KJ) bond is lower than that of Mn–O bond (bond enthalpy = 402 KJ), hence the dissociation of Mg doped compound occurs at lower temperature. In the undoped compound weight loss begins at T_1 (835 °C) (Figure 3). The weight losses between T_1 and T_2 temperature for all the compounds have been calculated and the weight loss is minimum for $x = 0.0$ while the loss is maximum for $x = 0.30$. The weight losses in the compounds are primarily due to oxygen loss in the structure. The phase transformation takes place at gradually decreasing temperature with the increase in Mg doping content. The temperature T_2 at which second transition occurs increased for $x = 0.05$ and after that it decreases as the Mg content increases. The transitions at T_1 and T_2 correspond to the formation of monoclinic Li_2MnO_3 and tetragonal spinel. Another transition has been found at T_3 for the compounds having $x = 0.0$ and 0.05 , as shown in Figure 3a,b and this is attributed to a reversible transition of a tetragonal spinel to cubic structure [13]. The temperature T_3 also decreases with increase in Mg content within the compositional range studied. Such reversible transition does not occur in the compounds above $x = 0.05$.

DTA traces for all samples are shown in Figure 4. The endothermic peak at transition temperature Td_1 corresponding to the formation of LiMnO_2 decreases as the Mg content increases in the doped structure. The temperature Td_2 also decreases with increase in

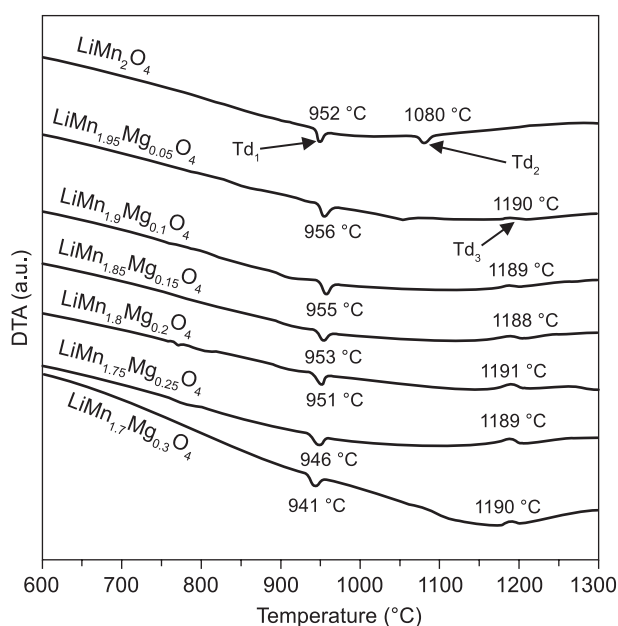
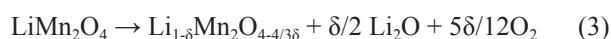


Figure 4. DTA plots of $\text{Li}[\text{Mn}_{2-x}\text{Mg}_x]\text{O}_4$ where $x = 0.00, 0.05, 0.10, 0.15, 0.20, 0.25, 0.30$.

Mg content up to $x = 0.05$. No such transformation can be seen for $x > 0.05$. Suppression of endothermic peak at Td_2 is probably due to stabilization of LiMnO_2 (orthorhombic) and Mn_3O_4 (tetragonal spinel) phases by Mg doping as reported in the literature [14, 15]. The temperature Td_3 corresponds to the replacement of Li^+ by Mn ions on the tetrahedral sites of the spinel with loss of lithium and oxygen [13]. The exothermic peak at this temperature does not appear in undoped sample but is present in all doped samples and the temperature corresponding to exothermic peak is almost same for all doping concentration. Overall reaction at around 1190°C is given by



IR spectra

In the disordered normal cubic spinel with space group O_h^7 , lithium ion occupies 8a sites with a point group symmetry T_d , transition metal ions occupy 16d sites which has D_{3d} symmetry and oxygen ions are in 32e sites with site symmetry C_{3v} [15]. For divalent metal ions substituted spinels ($\text{LiMn}_{2-x}\text{Mg}_x\text{O}_4$), the main structural feature is the ordering of M^{2+} : Mn^{4+} ions in the 16d octahedral sites which reduce the space group symmetry from O_h^7 (Fd3m) to O^7 (P4₃32). In case of disordered cubic spinel with space group of Fd3m only four infrared active modes exist [16].

The IR spectra of $\text{Li}[\text{Mn}_{2-x}\text{Mg}_x]\text{O}_4$ powders having compositions ($x = 0.0, 0.05, 0.1, 0.15, 0.2, 0.25$ and 0.3) are shown in Figure 5. The room temperature spectrum of LiMn_2O_4 mainly consists of two frequency bands centered at about wave numbers of 614 and 514 cm^{-1} corresponding to asymmetrical stretching modes of MnO_6 octahedrons [17, 18]. The third band is observed as weak shoulder on the lower wave number side at 435 cm^{-1} . Julien et al. [19] has shown that the vibration band at 450–650 cm^{-1} range corresponds to the octahedral symmetry of the ions. However, vibrational stretching modes in the wave number range 350–450 cm^{-1} are associated with the vibrations of lithium cations. Figure 5 shows that the band at 614 cm^{-1} for LiMn_2O_4 material is slightly shifted towards the higher wavenumber for $x \geq 0.2$. This may be due to the increase in population of Mn^{4+} in octahedral sites and absence of cation ordering. However for $x > 0.2$, FTIR study shows increase in the number of infrared ray active modes. The bands at higher wavenumber of 614 cm^{-1} starts splitting with the evolution of three new band at 557, 598 and 664 cm^{-1} for $x = 0.3$ and new bands have been also appeared at lower wavenumber side. Group theory analysis explained that with an increase in infrared active modes, the crystal symmetry decreases from Fd3m to P4₃32 [20] resulting in the formation of more ordered structure.

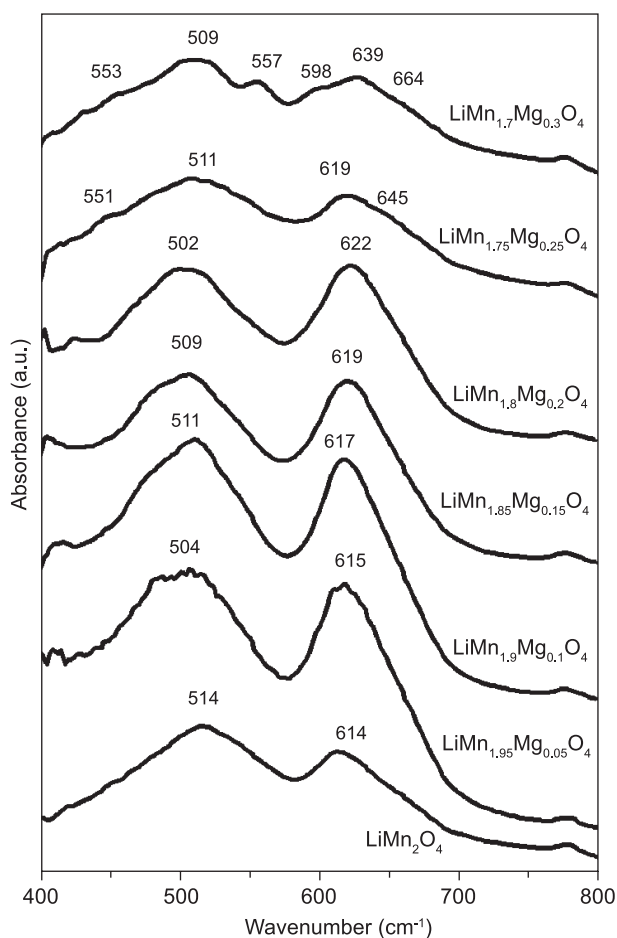


Figure 5. FTIR spectra of $\text{Li}[\text{Mn}_{2-x}\text{Mg}_x]\text{O}_4$ where $x = 0.00, 0.05, 0.10, 0.15, 0.20, 0.25, 0.30$.

Morphological studies

The morphology of the synthesized powders has been observed by field emission scanning electron microscopy (FE-SEM) and the micrographs are shown in Figure 6. It can be seen from the figure that the average particle size in case of the Mg doped samples is less compared to that of undoped LiMn_2O_4 . This might be explained on the basis of the fact that in this Mg doped system the drive for the nucleation have overcome that of the growth of the particles. Average particle size of the samples decreases with increase in x for $\text{Li}[\text{Mn}_{2-x}\text{Mg}_x]\text{O}_4$ ($x = 0.0, 0.05, 0.1, 0.15, 0.2, 0.25$ and 0.3) as obtained from the Image J software. From Figure 6, it is clear that the average particle size of LiMn_2O_4 is about 310-320 nm and as the of Mg content increases the average particle size decreases and the particle size becomes about 220 nm for $x = 0.3$. The shape of the particles is spherical dodecahedron for all the samples. The particles are in slightly agglomerated state which may be beneficial towards having good packing density of the material leading to higher bulk capacity [21].

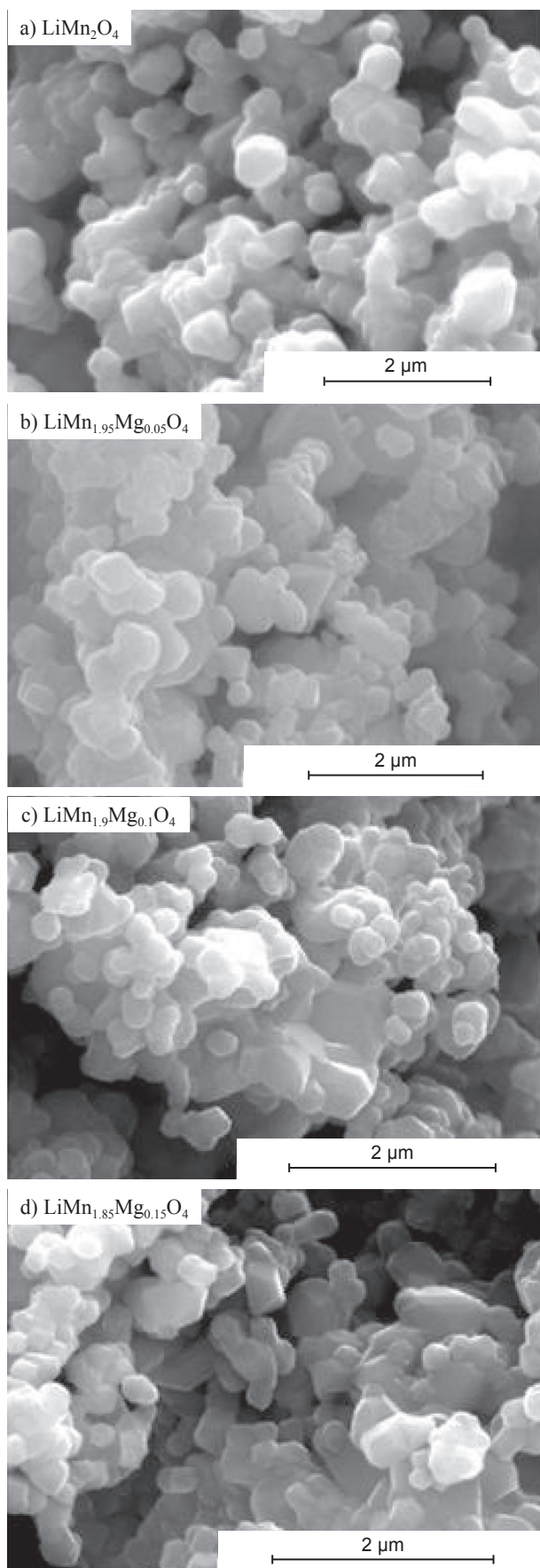


Figure 6. FESEM micrographs of the $\text{Li}[\text{Mn}_{2-x}\text{Mg}_x]\text{O}_4$ where $x = 0.00$ (a), 0.05 (b), 0.10 (c), 0.15 (d).

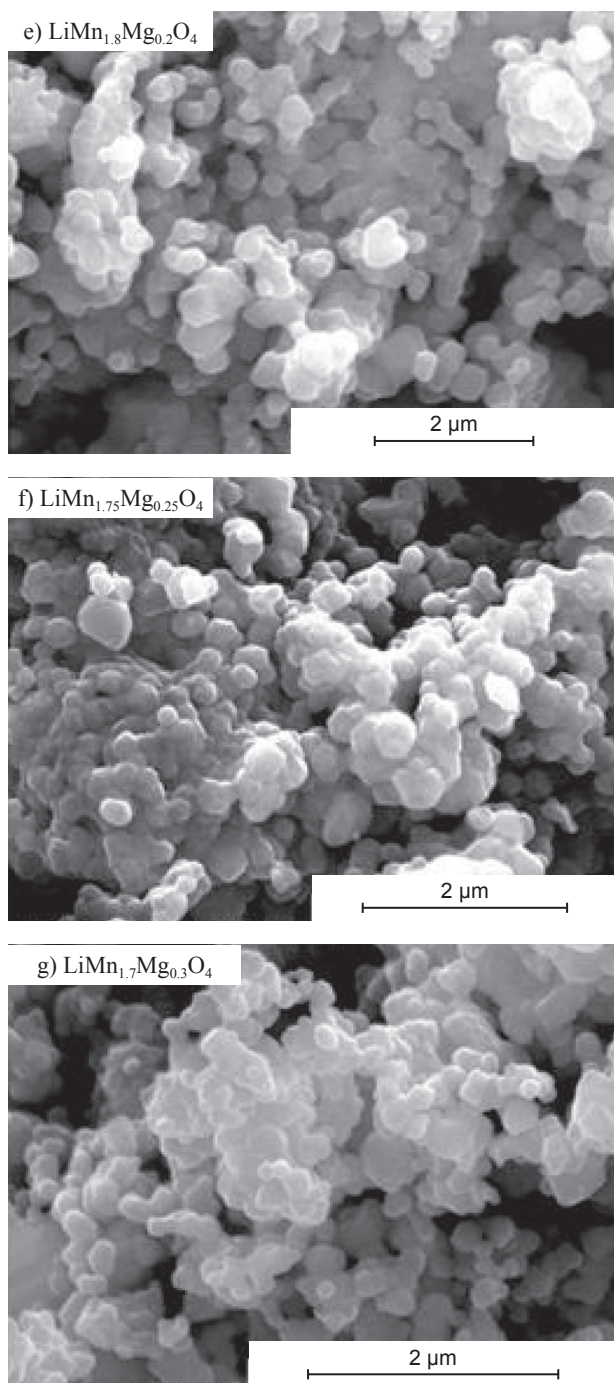


Figure 6. FESEM micrographs of the $\text{Li}[\text{Mn}_{2-x}\text{Mg}_x]\text{O}_4$ where $x = 0.20$ (e), 0.25 (f), 0.30 (g).

Electrochemical properties

Figure 7 shows the voltage vs charge and discharge capacity curves of $\text{Li}/\text{Li}[\text{Mn}_{2-x}\text{Mg}_x]\text{O}_4$ ($x = 0.0, 0.05, 0.15, 0.25$) powders in a voltage range of 3 V- 4.3 V. For LiMn_2O_4 there is voltage step at 4.05 V. Ohzuku et al. [22] however, observed the voltage step at 4.11 V and have attributed this to the transition from two cubic phases to a single cubic phase. This voltage step reduces

as the Mg content increases in the compound and it is completely vanished for $x = 0.25$, showing that the Mg doping in LiMn_2O_4 stabilizes the cubic-cubic transition in the crystal structure. The discharge capacity of LiMn_2O_4 is about 122 mAh/g. The capacity of Mg doped samples decreases with the increase in Mg content. Decrease in capacity of $\text{Li}[\text{Mn}_{2-x}\text{Mg}_x]\text{O}_4$ for $x = 0.05, 0.15$ and 0.25 is due to decrease in the lithium which is extractable. The removal of lithium from the spinel is accompanied by oxidation of Mn^{3+} to Mn^{4+} . The amount of removable lithium was determined by the Mn^{3+} content. So the content of Mn^{3+} reduces, thus only $(1-x)$ Li can be extracted from the spinel structure.

Figure 8 shows the discharge capacity versus cycle number of $\text{Li}/\text{Li}[\text{Mn}_{2-x}\text{Mg}_x]\text{O}_4$ ($x = 0.0, 0.05, 0.15, 0.25$) at a constant current of 100 mA and cutoff voltage from 3.0 V to 4.3 V. The discharge capacity of LiMn_2O_4 initially is 122 mAh/g which reduces to 111 mAh/g at the 10th cycle. It can be seen from Figure 8 that capacity of $\text{Li}[\text{Mn}_{2-x}\text{Mg}_x]\text{O}_4$ with $x = 0.0, 0.05$ and 0.15 decreases for the first 10 cycles. But decrease in capacity of doped compound is found less compared with undoped compound. This is due to the substitution of Mg^{2+} into the Mn site accompanied by the oxidation of Mn^{3+} into Mn^{4+} resulting in an increase in the average valency of Mn which suppresses the Jahn–Teller distortion. Li et al. [23] also reported that the doping enhances the stability of the octahedral sites in the spinel structure. While in the case of $\text{Li}[\text{Mn}_{2-x}\text{Mg}_x]\text{O}_4$ with $x = 0.25$ samples, the capacity continuously increases. The initial discharge capacity of $\text{Li}[\text{Mn}_{1.25}\text{Mg}_{0.25}]\text{O}_4$ is 61 mAh/g which has increased to 66 mAh/g after 10th cycle. Hence the Mg doping shows better capacity retention than that of LiMn_2O_4 , though the capacity reduces due to doping.

CONCLUSIONS

The following are the conclusions of the present work :

1. The synthesis of $\text{Li}[\text{Mn}_{2-x}\text{Mg}_x]\text{O}_4$ spinel compounds possess a single cubic spinel phase having space group $\text{Fd}\bar{3}\text{m}$ for the compositions ($x = 0.0, 0.05, 0.1, 0.15, 0.2$ and 0.25). However, the compound with $x = 0.30$, the coexistence of two space group $\text{Fd}\bar{3}\text{m}$ and $\text{P}4_3\bar{2}$ has been observed with cubic spinel structure.
2. TG analysis shows the transition temperature (T_1) which corresponds to the oxygen loss in the structure decreases as the Mg content in the compound increases, clearly showing that the oxygen loss from the structure begins at lower temperature.
3. Suppression of endothermic peak at T_{d2} temperature in DTA graph shows the stabilization of the orthorhombic LiMnO_2 and tetragonal Mn_3O_4 phases.
4. FTIR spectrum of the compound for $x = 0.3$ has more allowed modes showing the structure is more ordered than undoped spinel.

5. The average particle size of LiMn_2O_4 is about 310-320 nm and in the doped compounds, as the Mg content increases the average particle size decreases. The particle size becomes 220 nm for $x = 0.3$.
6. The voltage step which corresponds to cubic to cubic phase transition decreases in the doped compounds with the increase in Mg content. The voltage step gets completely eliminated for $x = 0.25$.
7. The discharge capacity of LiMn_2O_4 is about 122 mAh/g. The capacity of the doped compounds decreases with increase in the Mg content. Capacity retention improves in rechargeable 4V Li/Li $[\text{Mn}_{2-x}\text{Mg}_x\text{O}_4]$ cells for Mg doped compounds.

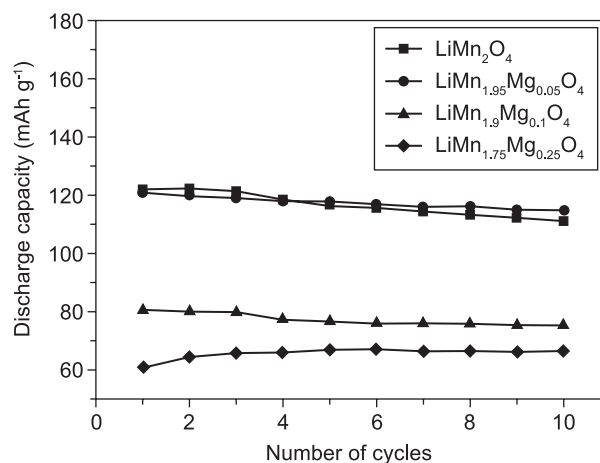


Figure 8. Cyclic performance of Li cells.

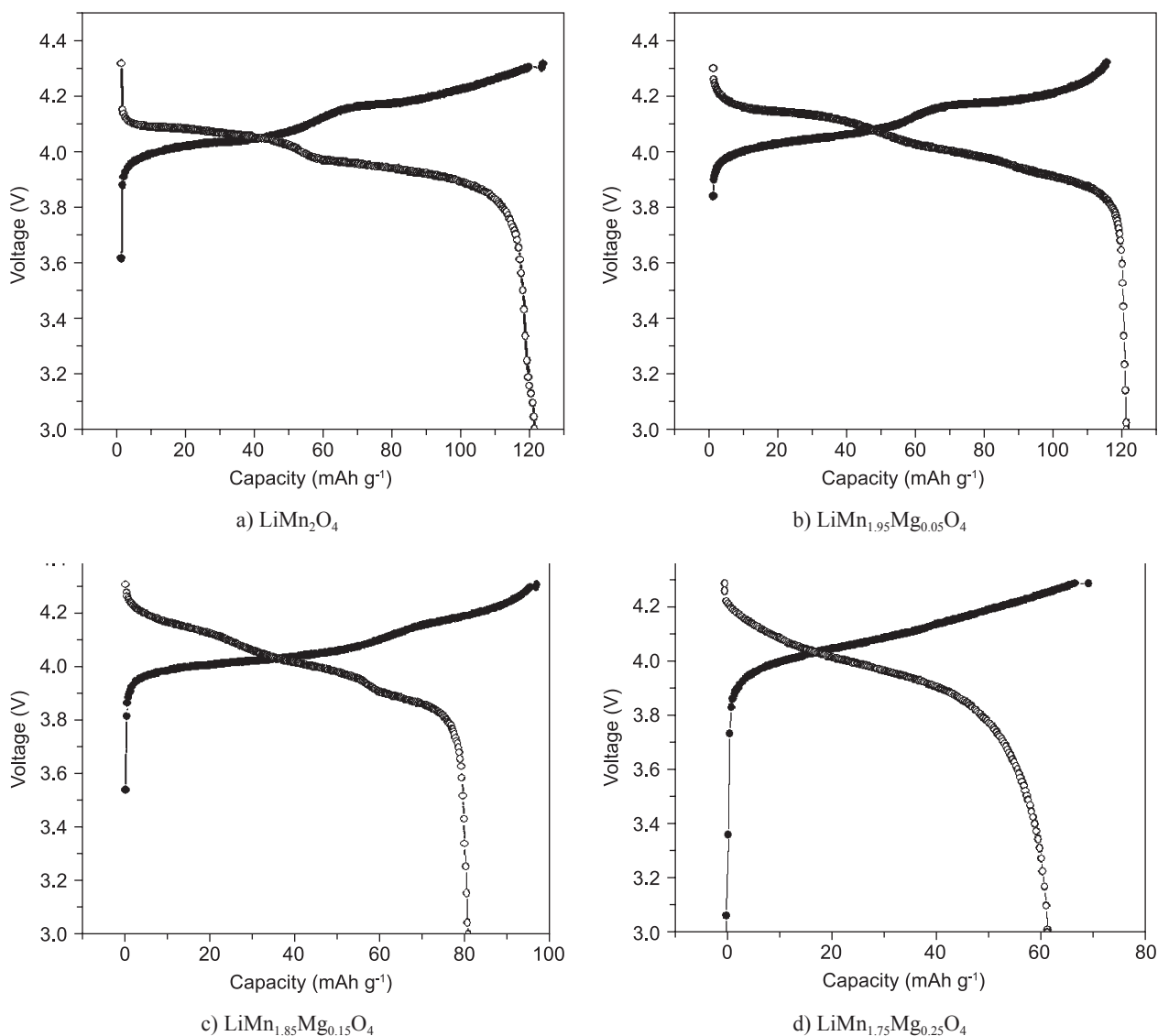


Figure 7. First charge and discharge curves of Li cells (● - charging curve, ○ - discharging curve).

References

1. Basu S.: US patent, 4,304,825 (1981).
2. Goodenough J.B., US patent, 4,357, 215 (1992).
3. Amatucci G.G., Tarascon J.M., Klein L.C.: *J. Electrochem. Soc.* *143*, 1114 (1996).
4. Peramunage D., Abraham K.M.: *J Electrochem. Soc.* *145*, 1132 (1998).
5. Yamada A.: *J. Solid State Chem.* *122*, 160 (1996).
6. Jang D. H., Shin J.Y., Oh S.M.: *J. Electrochem. Soc.* *143*, 2204 (1996).
7. Goodenough J. B., Thackeray M. M., David W. I. F., Bruce P. G.: *J. Solid State Chem.* *67*, 316 (1987).
8. Thackeray M. M., Picciotto L., Kock A. de, Johnson P. J., Nicholas V., Adendorff K.: *J. Power Sources* *21*, 1 (1987).
9. Min Y. Z. and Lian-cheng Z.: *J. Trans Nonferrous Mat. Soc China* *17*, 659 (2007).
10. Thackeray M. M.: *J. Prog. Solids. Chem.* *25*, 1 (1997).
11. Sigh G., Sil A., Ghosh S.: *Physica B* (2009) Doi:10.1016/j.physb.2009.06.148.
12. Gummow R.J., Kock A. de, Thackeray M.M.: *J. Solid State Ionics* *69*, 59 (1994).
13. Thackeray M.M., Mansuetto M.F., Dees D.W., Vissers D. R.: *J. Materials Research Bulletin* *31*, 133 (1996).
14. Tsuji T., Umakoshi H., Yamamura Y.: *J. Physics and Chemistry of Solids* *66*, 283 (2005).
15. Yamaguchi R., Ikuta H., Wakihara M.: *J. Therm. Anal. Calorim.* *57*, 797 (1999).
16. White W. B., Deangelis B. A.: *J. Spectrochimica. Acta* *23A*, 985 (1967).
17. Zwinscher J., Gupta H. C., Lutz H. D.: *J. Phys. Chem. Solids* *55*, 287 (1994).
18. Lutz H. D., Muller B., Steiner H. J.: *J. of Solid State Chemistry* *90*, 54 (1991).
19. Julien C.M., Massot M.: *Materials Science and Engineering B* *100*, 69 (2003).
20. Allen G. C. and Paul M.: *J. of Applied Spectroscopy* *49*, 451 (1994).
21. Thirunakaran R., Kim Ki-Tae, Kang Yong-Mook, Lee J. Y.: *J. Materials Research Bulletin* *40*, 177 (2005).
22. Ohzuku T., Kitagawa M., Hirai T.: *J. Electrochem. Soc.* *137*, 769 (1990).
23. Guohua Li., Ikuta H., Uchida T., Wakihara M.: *J. Electrochem. Soc.* *143*, 178 (1996).